Electronic Supplementary Material (ESI) for Journal of Materials Chemistry A.

Electronic Supplementary Information

Nanopillar-Structured Perovskite-Based Efficient Semitransparent Solar Module for Power-Generating Window Applications

Hyeok-Chan Kwon, Sunihl Ma, Seong-Cheol Yun, Gyumin Jang, Hyunha Yang, and Jooho Moon*

Department of Materials Science and Engineering, Yonsei University

50 Yonsei-ro Seodaemun-gu, Seoul 03722, Republic of Korea

Email: jmoon@yonsei.ac.kr

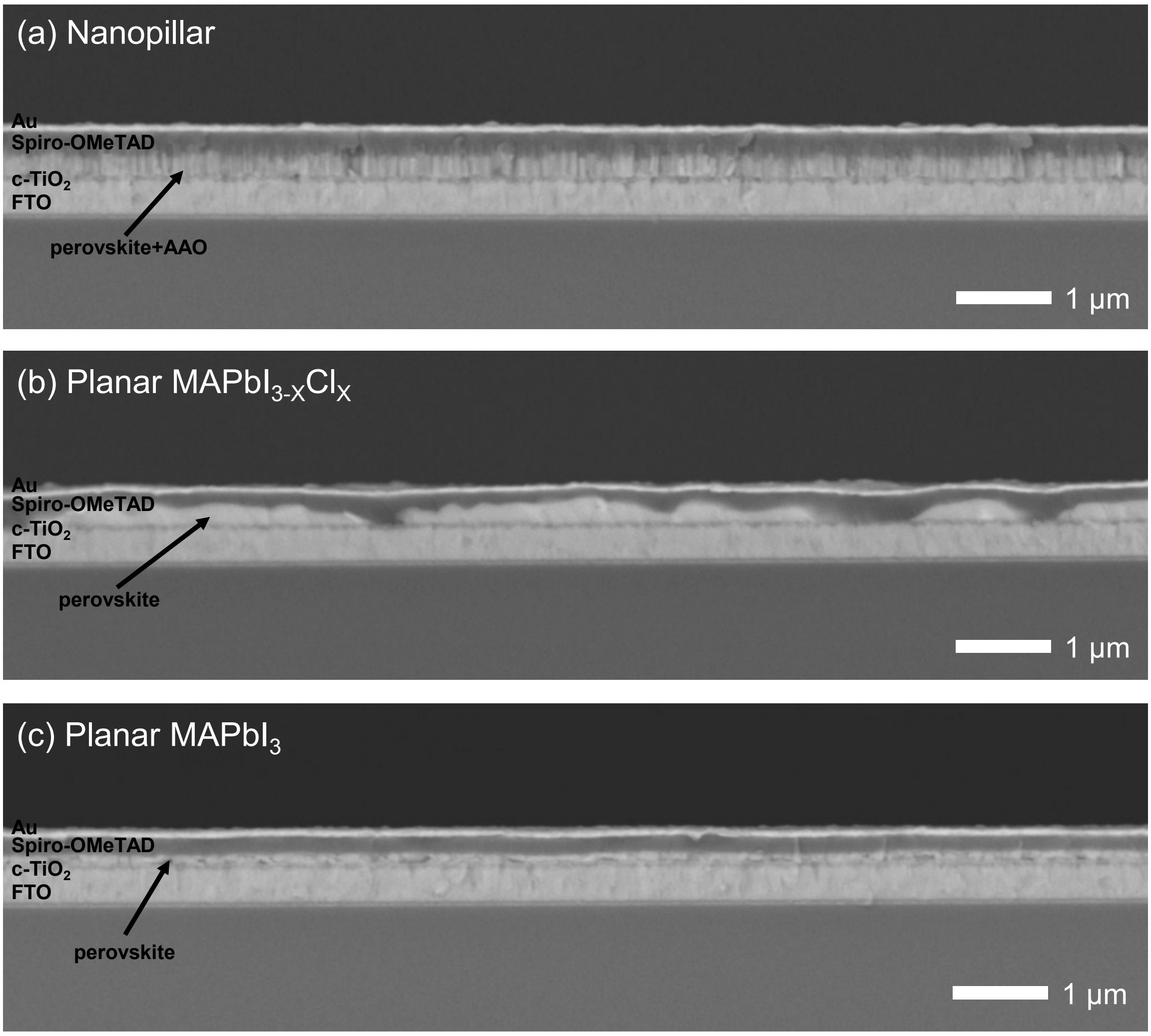

Fig. S1 Cross-sectional SEM images of the nanopillar, planar $MAPbI_{3-X}Cl_X$, and planar $MAPbI_3$ perovskite solar cells.

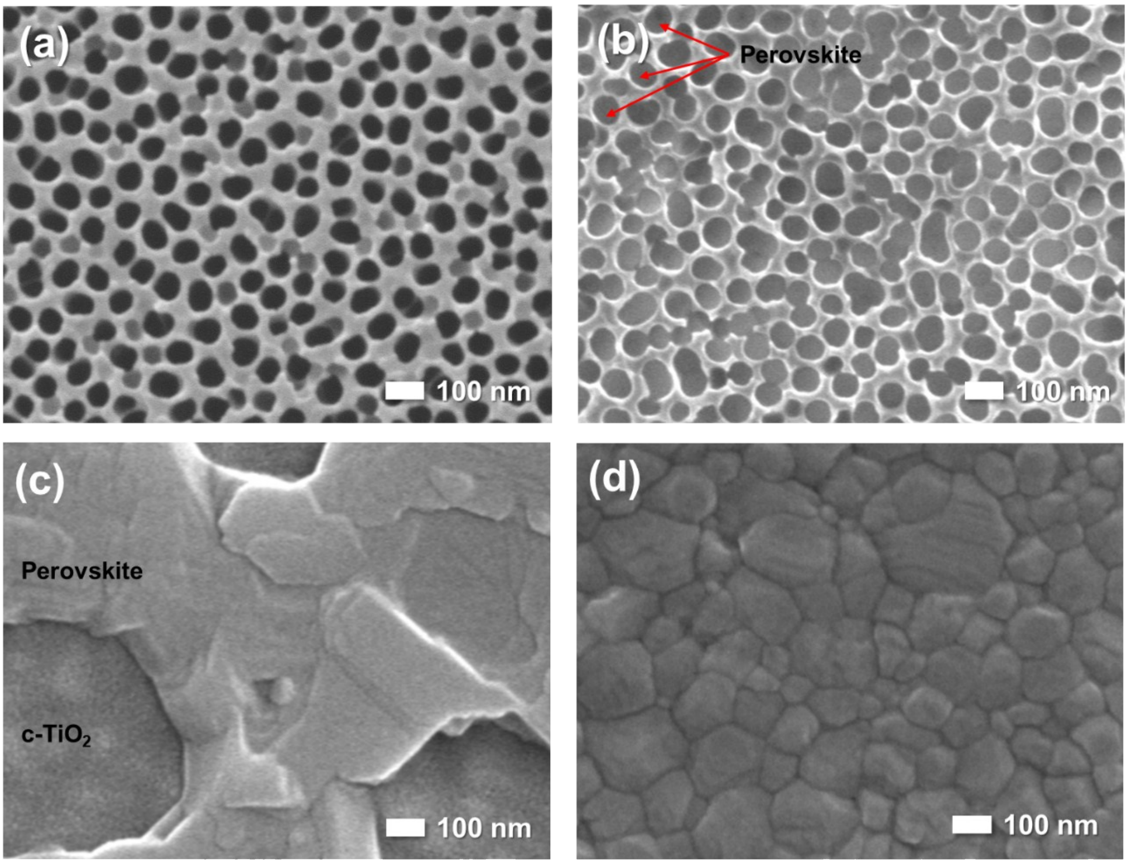

Fig. S2 Surface SEM image of (a) empty AAO on top of compact TiO_2, (b) the perovskite infiltrated into AAO scaffold, (b) planar $MAPbI_{3-X}Cl_X$ perovskite on top of compact TiO_2, and (c) planar $MAPbI_3$ perovskite on top of TiO_2.

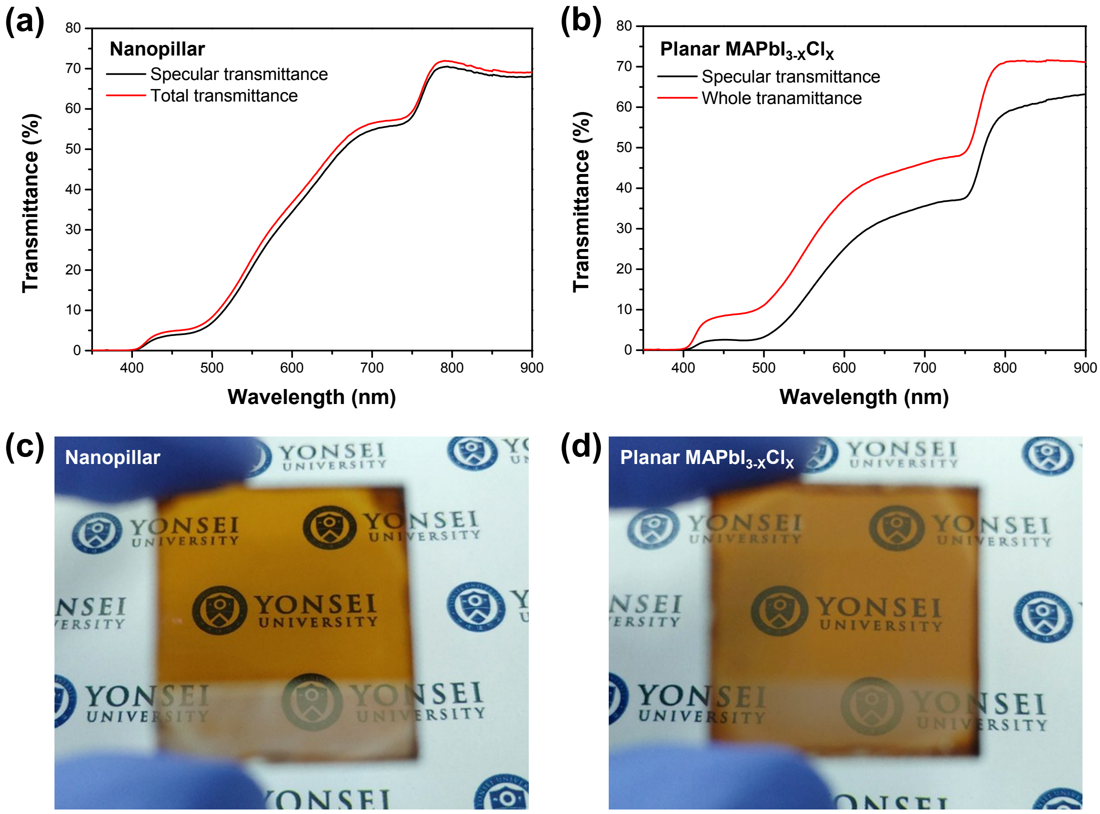

Fig. S3 Specular- and total-transmittance spectra of (a) nanopillar- and (b) planar-structured perovskite with a configuration of spiro-OMeTAD/perovskite+(AAO)/c-TiO_2/FTO/glass. Photographs of (c) nanopillar- and (d) planar-structured perovskite cells.

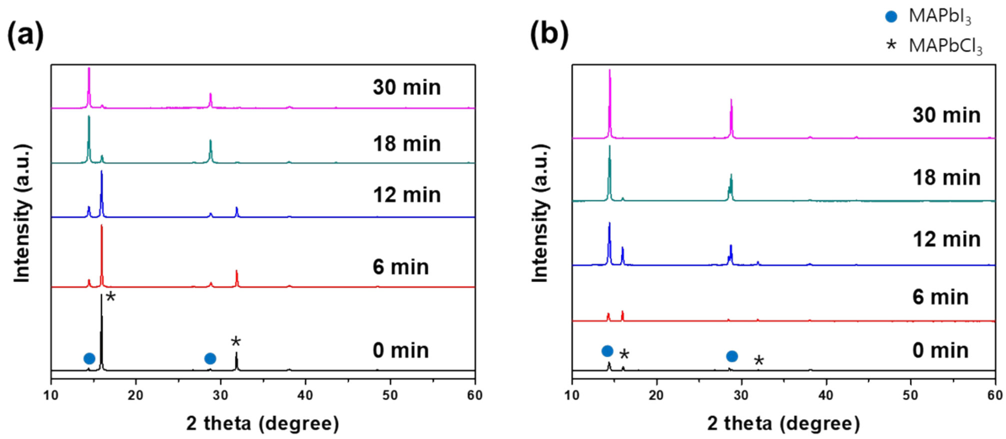

Fig. S4 XRD spectra for (a) AAO based nanopillar perovskite and (b) planar perovskite as a function of annealing time from 0 min (as-prepared) to 30 min.

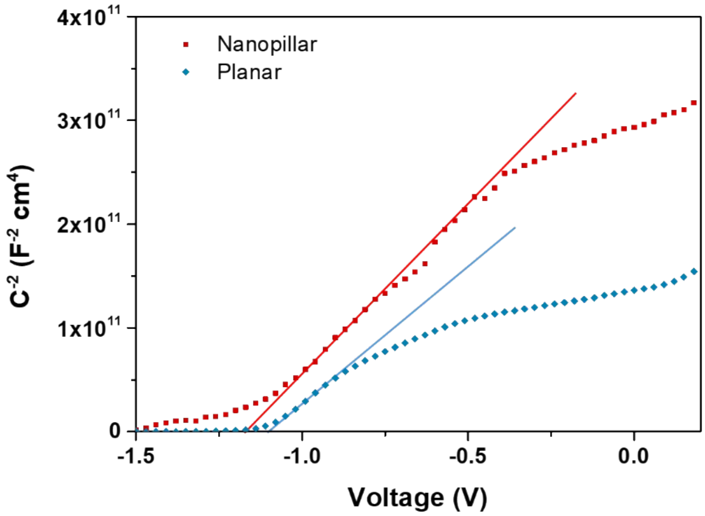

Fig. S5. Mott-Schottky plot for nanopillar and planar structured perovskites under dark condition and 10 kHz voltage frequency.

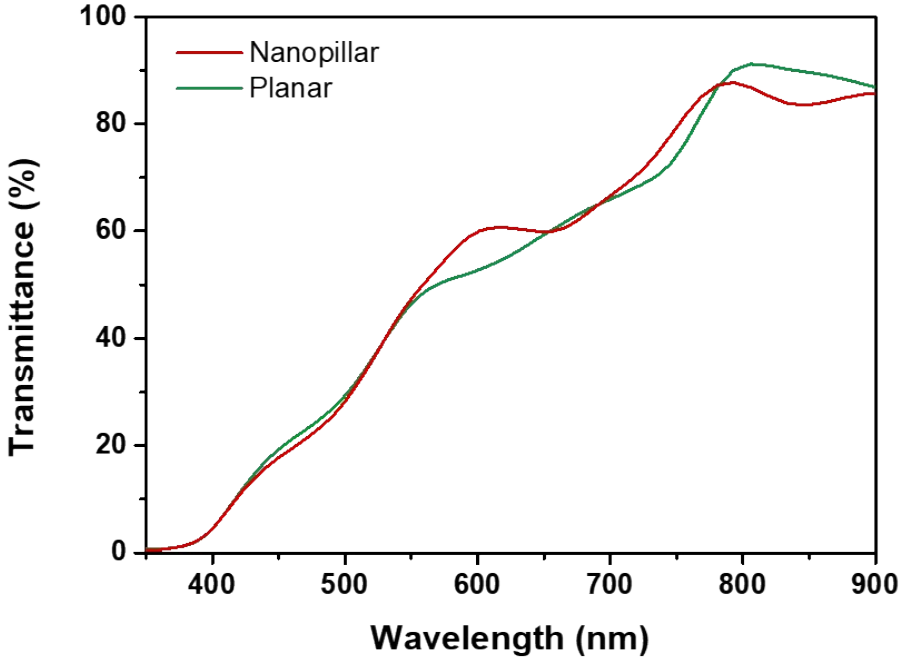

Fig. S6 Transmittance spectra from the FDTD optical simulation results for the nanopillar- and planar-structured perovskite solar cells.

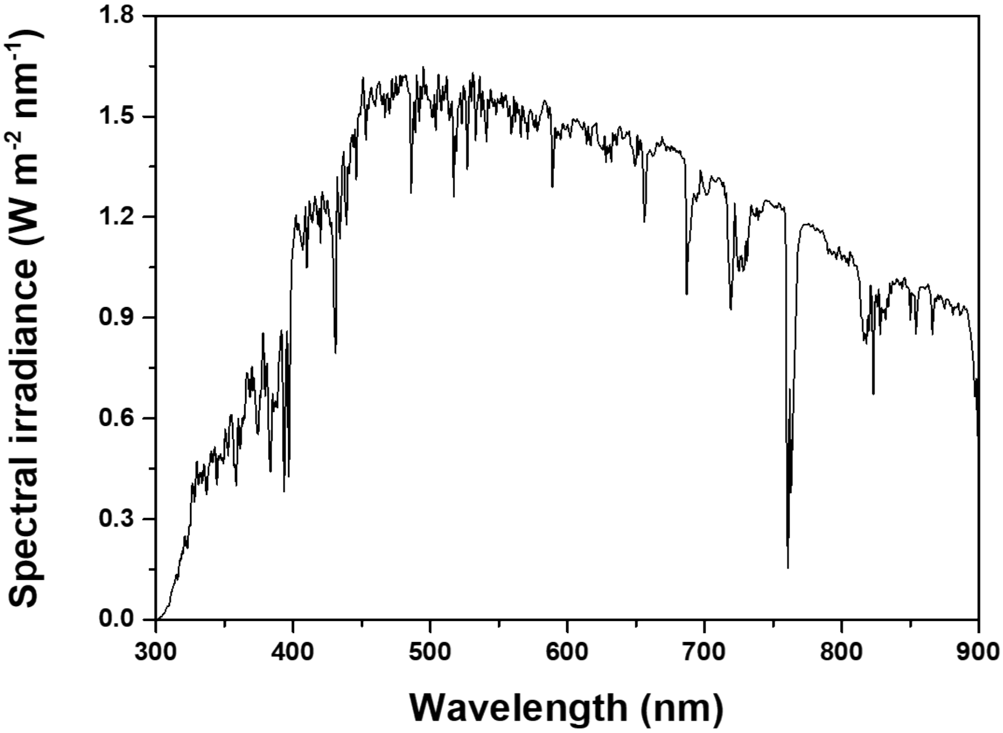

Fig. S7 Standard solar spectral irradiance spectrum at AM 1.5G with an integrated power of 100 mW/cm^2.

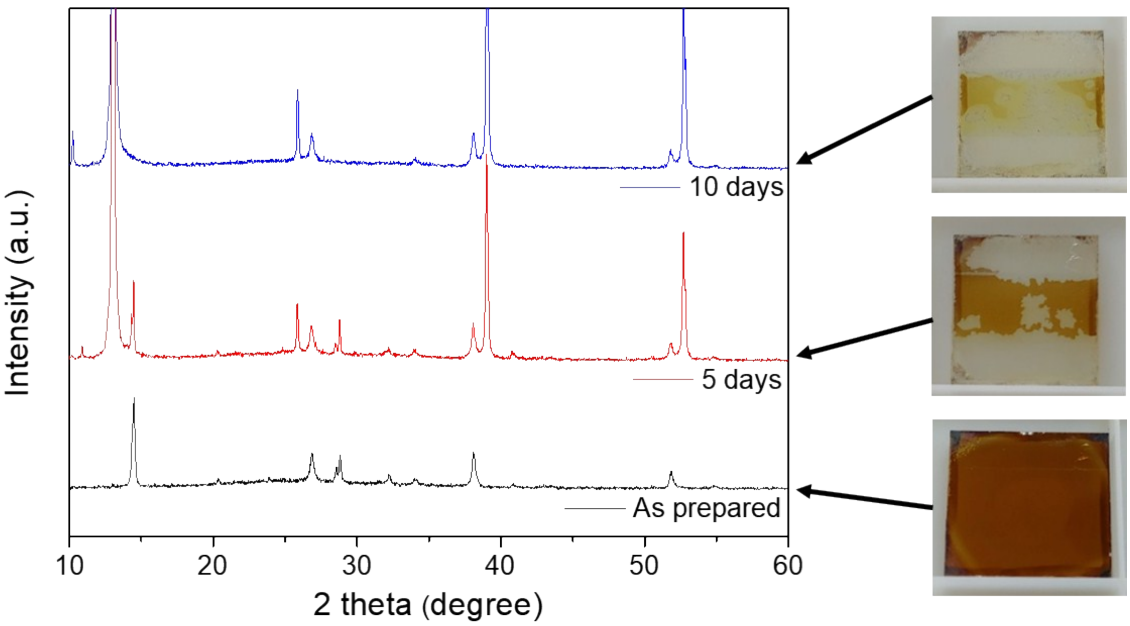

Fig. S8 XRD patterns of the planar-structured $MAPbI_3$ device with a configuration of spiro-OMeTAD/perovskite/c-TiO_2/FTO/glass after storage for 0 (as-prepared), 5, and 10 days.

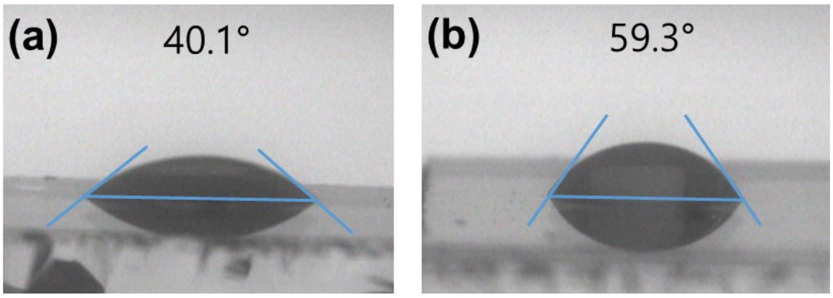

Fig. S9. Contact angle of water droplets placed on (a) TiO_2/FTO and (b) AAO/TiO_2/FTO substrate.

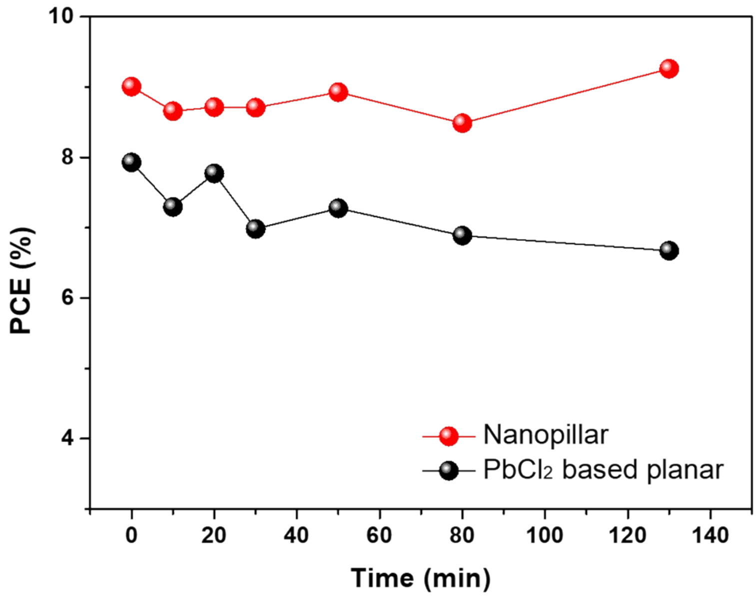

Fig. S10. Thermal stability behavior of nanopillar and planar $MAPbI_{3-X}Cl_X$ solar cells under 85 ^oC at the ambient air.

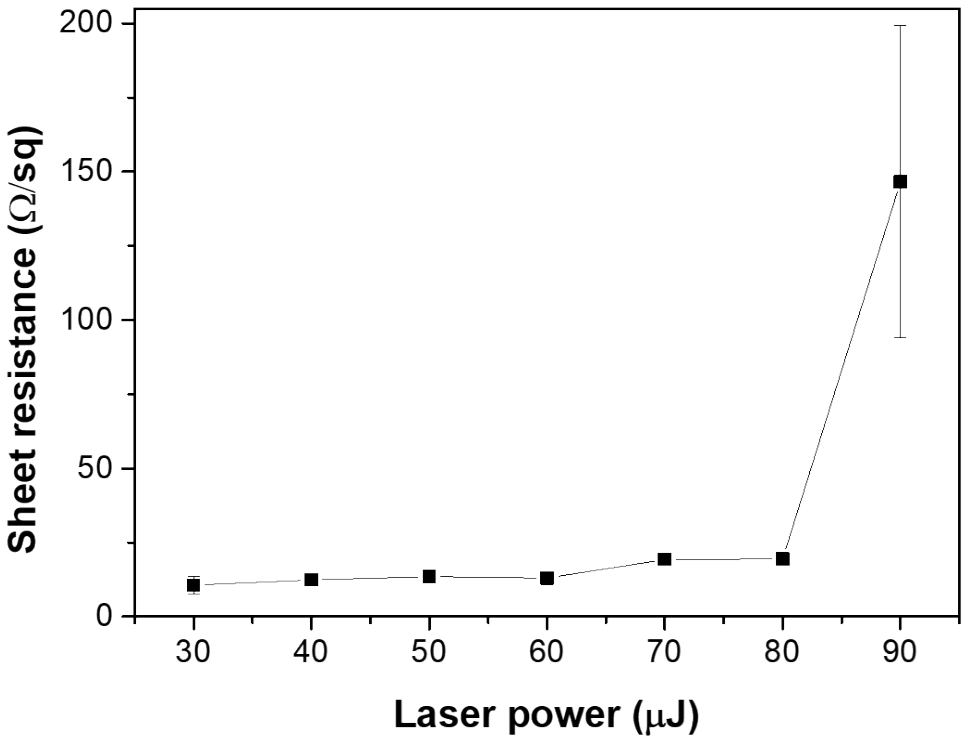

Fig. S11 Sheet-resistance variations of FTO after the laser scribing of the spiro-OMeTAD/perovskite+AAO/c-TiO_2/FTO/glass substrates, with respect to the laser power.

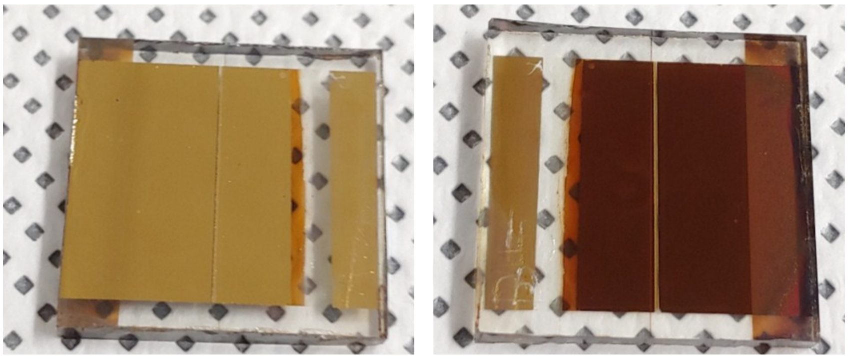

Fig. S12 Photographs of the mini-module with two sub-cells and an aperture area of 1.58 cm^2: top view (left) and bottom view (right).

Table S1 Performance parameters of the mini-module with respect to the laser power for P2 etching.

Laser power		V_{OC} (V)	J_{SC} (mA/cm^2)	FF (%)	PCE (%)
35 μJ	champion	2.20	6.80	65.67	9.84
	average	2.08 ± 0.23	5.87 ± 1.76	53.83 ± 16.68	7.14 ± 3.41
50 μJ	champion	2.23	6.71	68.93	10.31
	average	2.00 ± 0.43	6.60 ± 0.22	58.09 ± 13.88	8.07 ± 3.00
65 μJ	champion	2.22	7.15	67.48	10.73
	average	2.21 ± 0.01	7.08 ± 0.08	64.84 ± 5.94	10.13 ± 0.87
80 μJ	champion	2.23	6.95	69.39	10.73
	average	2.20 ± 0.03	6.92 ± 0.25	64.85 ± 5.33	9.88 ± 0.91

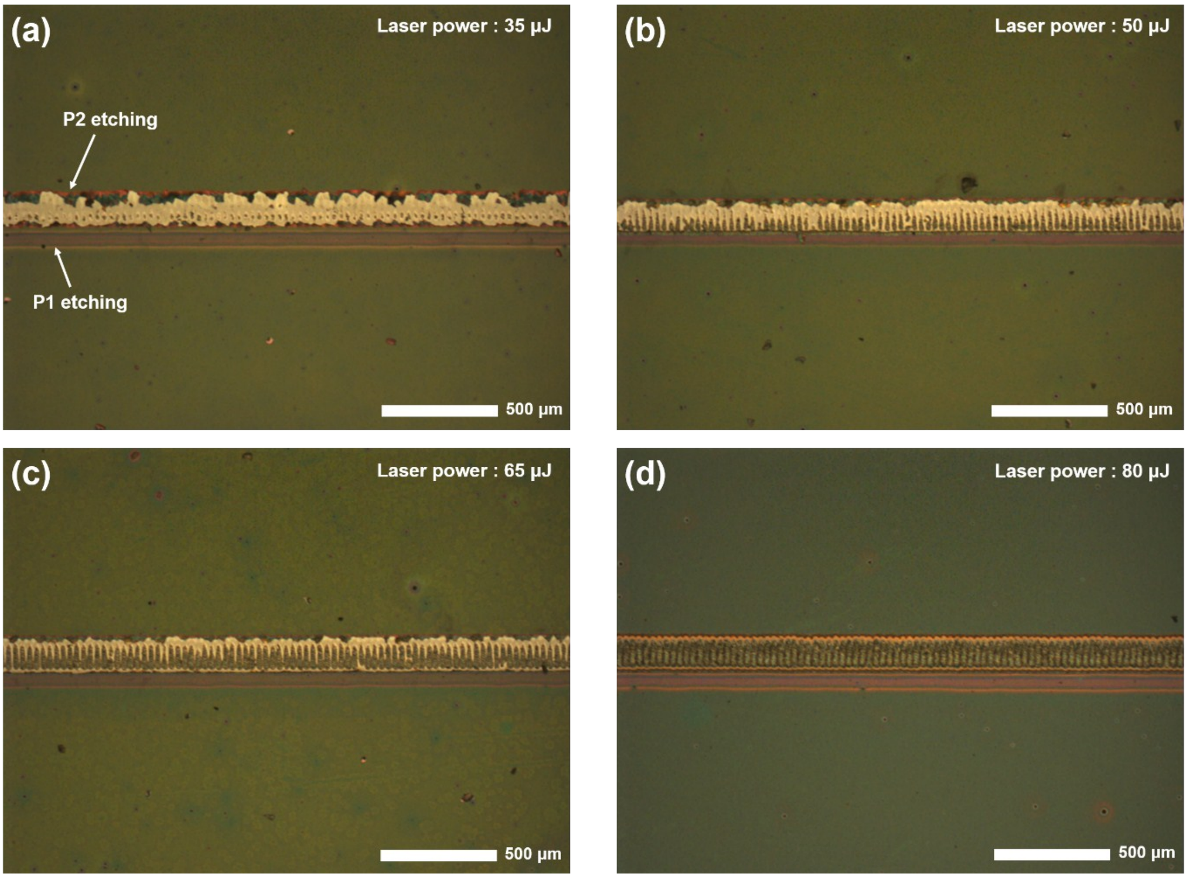

Fig. S13 The optical microscope images showing the surfaces of the solar module after P2 etching as a function of laser powers of (a) 35, (b) 50, (c) 65, and (d) 80 μJ.

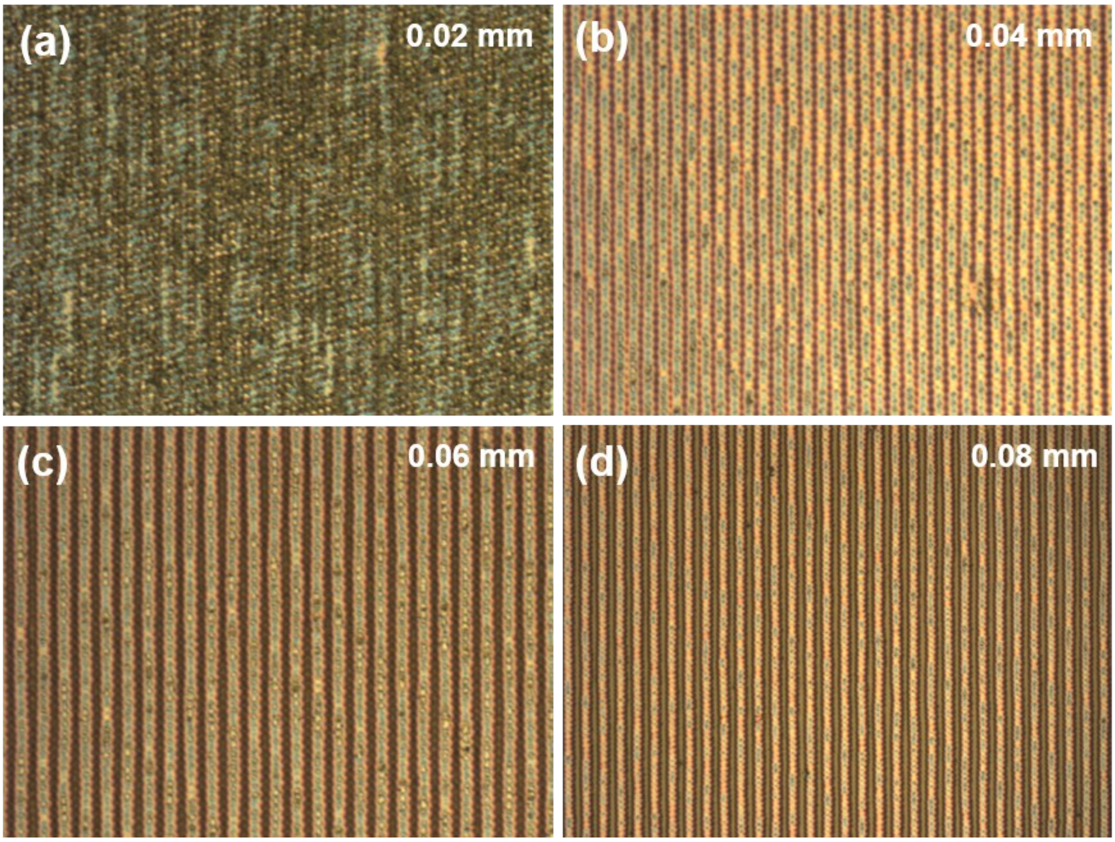

Fig. S14 Optical microscope images showing the surfaces of the solar module after laser etching of the spiro-OMeTAD/perovskite+AAO/c-TiO_2/FTO/glass substrates, with respect to the laser-scanning line interval: (a) 0.02, (b) 0.04, (c) 0.06, and (d) 0.08 mm.

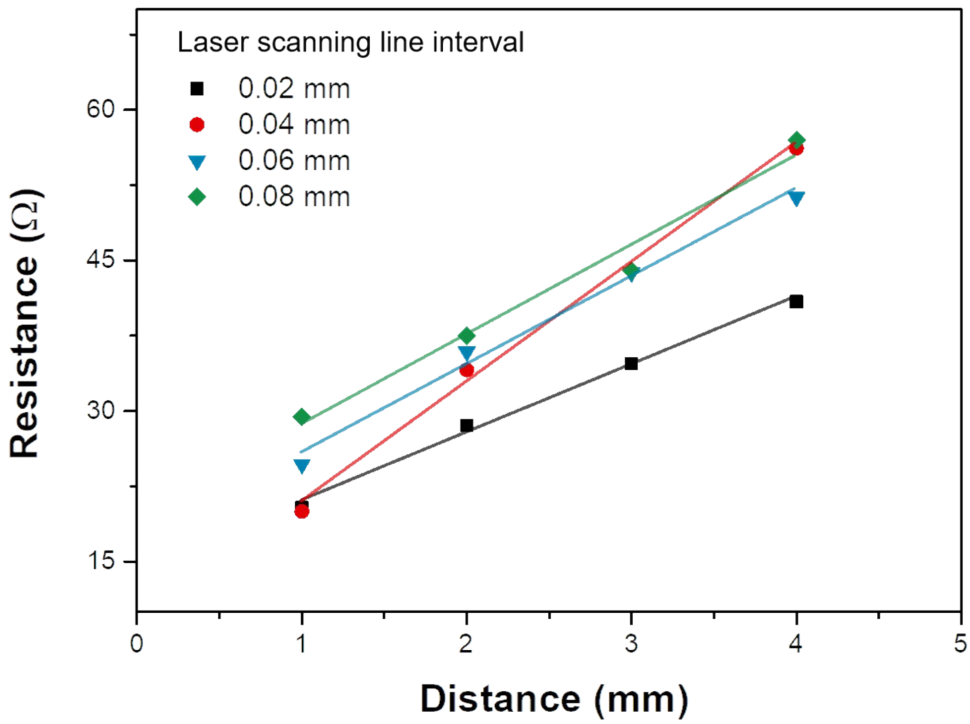

Fig. S15 Resistance with respect to the contact distance for TLM measurements using different laser-scanning line intervals.

Table S2 Performance parameters of the mini-module with respect to the laser-scanning line interval for P2 etching.

Laser scanning line interval (mm)		V_{OC} **(V)**	J_{SC} **(mA/cm²)**	**FF (%)**	**Efficiency (%)**
0.02	champion	2.24	6.55	70.34	10.31
	average	2.19 ± 0.05	6.19 ± 0.26	68.06 ± 1.62	9.25 ± 0.77
0.04	champion	2.28	6.65	68	10.32
	average	2.19 ± 0.07	6.23 ± 0.50	67.78 ± 1.04	9.25 ± 0.95
0.06	champion	2.26	6.33	66.05	9.44
	average	2.17 ± 0.06	5.99 ± 0.37	62.70 ± 2.44	8.19 ± 0.99
0.08	champion	2.23	6.37	64.56	9.16
	average	2.16 ± 0.07	5.86 ± 0.37	65.13 ± 0.69	8.26 ± 0.75

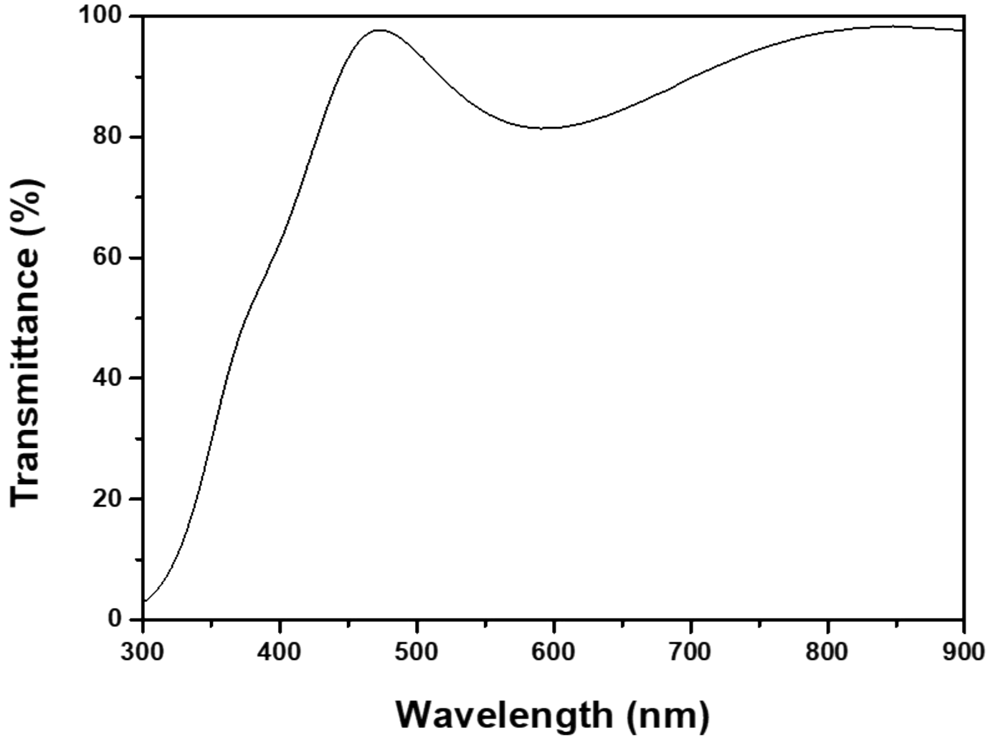

Fig. S16 Transmittance spectrum of the ITO sputtered on the glass.

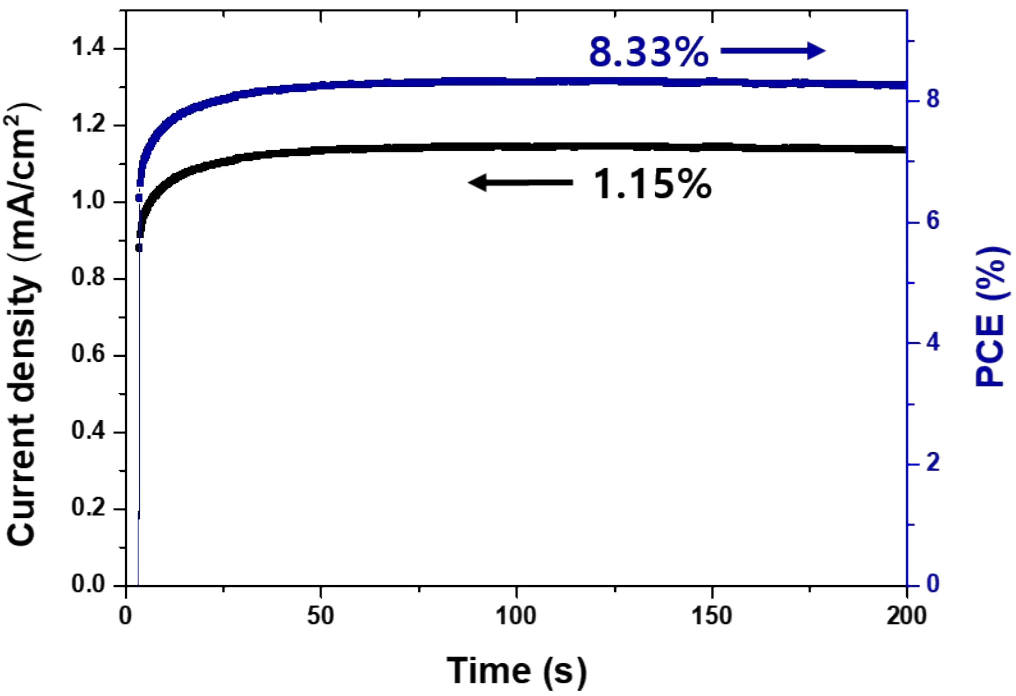

Fig. S17 Stabilized PCE of the semitransparent solar module with an aperture size of 40.8 cm^2 under constant 1-sun (100 mW/cm^2) illumination.

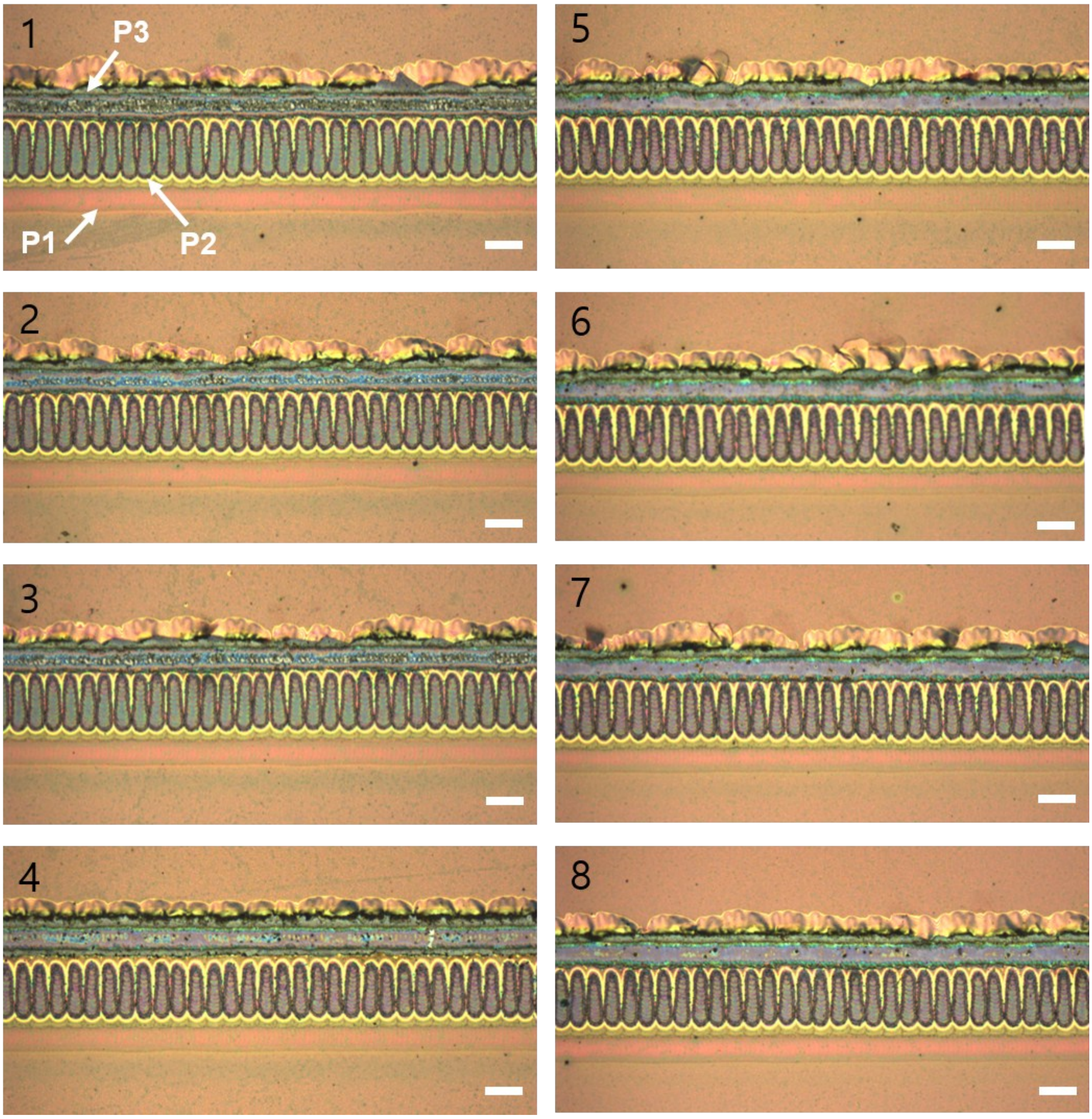

Fig. S18 Optical microscope images showing the eight dead areas in the semitransparent solar module after P1, P2, and P3 etchings for serially interconnecting the nine sub-cells.

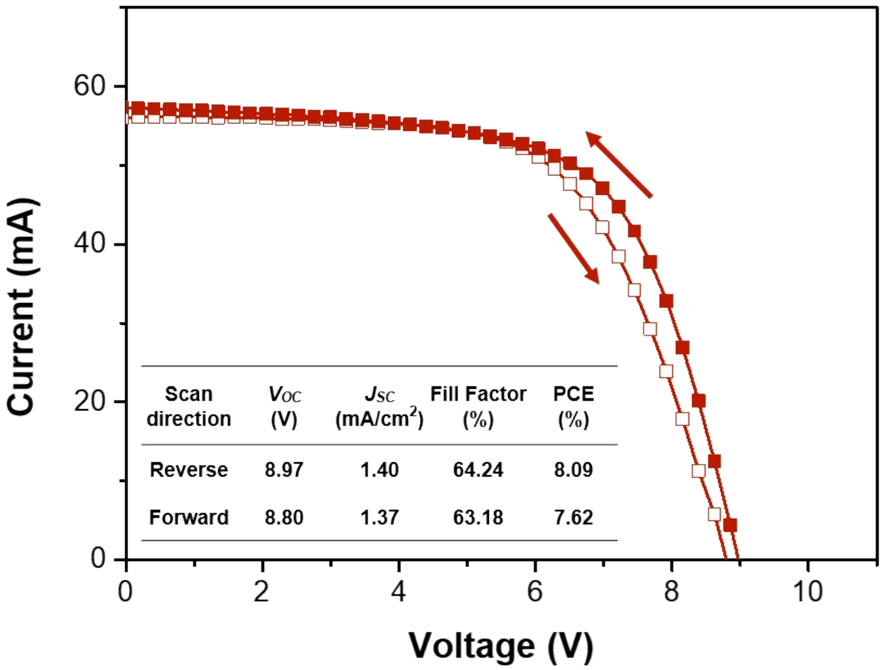

Fig. S19 *J*-*V* hysteresis characteristics of the semitransparent solar module based on nanopillar structured perovskite with a dwell time of 50 ms.

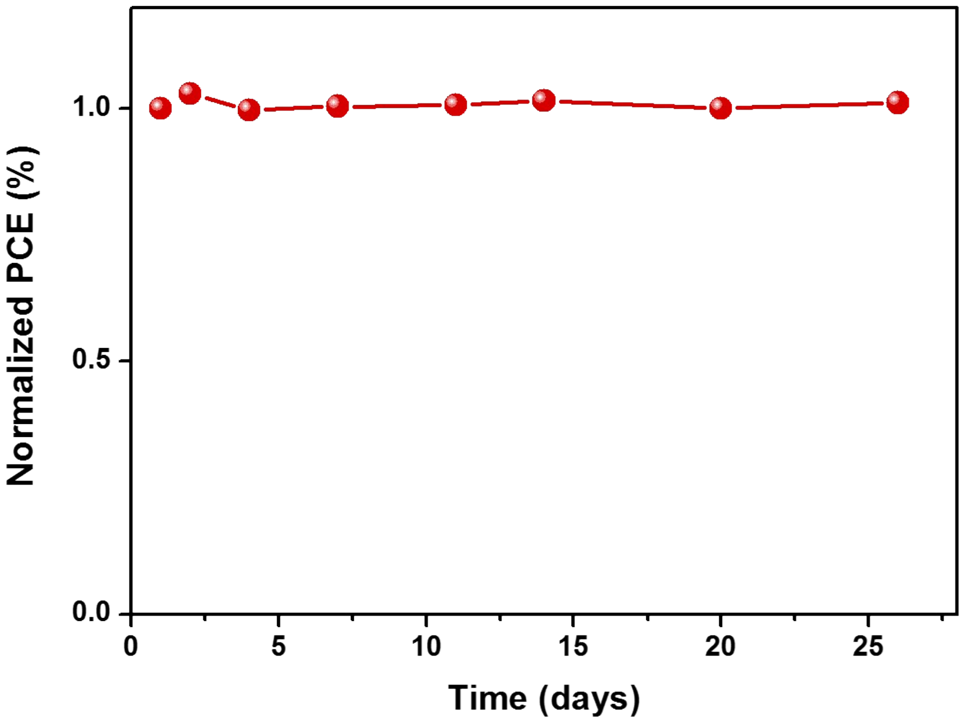

Fig. S20 Shelf stability of the semitransparent solar module without encapsulation stored in a dry-air atmosphere.

Table S3. Summary of semitransparent and large area solar cell/module.

Reference	Light absorber	Area (cm^2)		Transmittance: Average transmittance (%)	Transmittance: Wavelength range	Power conversion efficiency (%)
S1	P3HT:PCBM	30.00	active area	30.0	visible-near IR range	1.80
S2	a-Si:H/μc-Si:H tandem	100.00	aperture area	20.0	400-800 nm	6.50
S3	P3HT:PCBM	12.00	active area	-	-	2.44
S4	Perovskite	11.70	active area	(Almost opaque)	-	14.96
S5	PTB7-Th:PC71BM	216.00	active area	10.0	-	4.50
S6	P3HT:PCBM	6.00	active area	-	-	1.84 1.35 0.92
S7	PBDTTT-EFT:PC71BM	10.08	active area	14.0	400-700 nm	3.80
				10.0	400-700 nm	5.30
S8	pDPP5T-2:PC 60 BM	64.00	aperture area	56.8	at 550 nm	2.34
S9	PBTZT-stat-BDTT-8:PCBM:PEDOT:PSS	197.40	active area	10.0	380-780 nm	4.80
		68.76	active area	15.0	380-780 nm	4.30
S10	P3HT:PCBM	156.00	aperture area	-	-	1.15
This work	Perovskite	**40.80**	aperture area	**30.2**	400-800 nm	**9.04**

ESI references

S1 J. E. Lewis, E. Lafalce, P. Toglia and X. M. Jiang, *Sol. Energy Mat. Sol. C*, 2011, **95**, 2816-2822.

S2 G. M. Ablayev, A. I. Kosarev, A. V. Kukin, M. Y. Semerukhin, M. Z. Shvarts, E. I. Terukov and D. V. Zhilina, *J. Phys. Conf. Ser.*, 2014, **572**, 012049.

S3 Y. C. Huang, C. W. Chou, D. H. Lu, C. Y. Chen and C. S. Tsao, *IEEE J. Photovolt.*, 2018, **8**, 144-150.

S4 K. M. Lee, K. S. Chen, J. R. Wu, Y. D. Lin, S. M. Yu and S. H. Chang, *Nanoscale*, 2018, **10**, 17699-17704.

S5 K. M. Huang, Y. Q. Wong, M. C. Lin, C. H. Chen, C. H. Liao, J. Y. Chen, Y. H. Huang, Y. F. Chang, P. T. Tsai, S. H. Chen, C. T. Liao, Y. C. Lee, L. Hong, C. Y. Chang, H. F. Meng, Z. Y. Ge, H. W. Zan, S. F. Horng, Y. C. Chao and H. Y. Wong, *Prog. Photovol.*, 2019, **27**, 264-274.

S6 L. La Notte, D. Mineo, G. Polino, G. Susanna, F. Brunetti, T. M. Brown, A. Di Carlo and A. Reale, *Energy Technol.*, 2013, **1**, 757-762.

S7 Y. Q. Wong, H. F. Meng, H. Y. Wong, C. S. Tan, C. Y. Wu, P. T. Tsai, C. Y. Chang, S. F. Horng and H. W. Zan, *Org. Electron.*, 2017, **43**, 196-206.

S8 F. Guo, P. Kubis, T. Przybilla, E. Spiecker, A. Hollmann, S. Langner, K. Forberich and C. J. Brabec, *Adv. Energy Mater.*, 2015, **5**, 1601779.

S9 L. Lucera, F. Machui, H. D. Schmidt, T. Ahmad, P. Kubis, S. Strohm, J. Hepp, A. Vetter, H. J. Egelhaaf and C. J. Brabec, *Org. Electron.*, 2017, **45**, 209-214.

S10 Y. Galagan, H. Fledderus, H. Gorter, H. H. 't Mannetje, S. Shanmugam, R. Mandamparambil, J. Bosman, J.-E. J. M. Rubingh, J.-P. Teunissen, A. Salem, I. G. de Vries, R. Andriessen and W. A. Groen, *Energy Technol.*, 2015, **3**, 834-842.